ELSEVIER

International Journal of Heat and Fluid Flow 21 (2000) 684–692

International Journal of HEAT AND FLUID FLOW

www.elsevier.com/locate/ijhff

Heat transfer experiments in rotating boundary layer flow

Yoshihiro Edo, Shinnosuke Obi, Sigeaki Masuda *

Department of Mechanical Engineering, Keio University, 3-14-1 Hiyoshi, Kohoku-ku, Yokohama 223-8522, Japan

Received 27 November 1998; accepted 19 May 2000

Abstract

The influence of Coriolis force on heat transfer in a rotating transitional boundary layer has been experimentally investigated. The experiments have been conducted for local Görtler numbers up to 150. Heat transfer measurements have been performed for a flat plate with nearly uniform heat flux applied to the surface, where the temperature was measured by the thermochromic liquid crystal method. The results indicate that heat transfer is enhanced when Coriolis force acts towards the wall, i.e., on the pressure surface. The velocity measurements under equivalent conditions show that Coriolis instability induces counter-rotating longitudinal vortices which augment the lateral transport of the fluid on the pressure surface. On the other hand, the heat transfer on the suction surface remains at the same level as compared to the case without system rotation. As a consequence, the heat transfer coefficient on the pressure surface is 1.8 times higher than that measured on the suction surface when averaged over the measured surface.

Keywords: Heat transfer; Transitional boundary layer; Coriolis force; Thermochromic liquid crystal; Longitudinal vortex

1. Introduction

The heat transfer in a rotating system subjected to Coriolis force is of great engineering importance, particularly for designing rotational machinery, e.g., turbine blades, electrical machinery and generator rotors. Measurements of heat transfer under the influence of Coriolis force and investigation of the associated mechanism in relation to the Coriolis instability are desired.

Fig. 1 shows the conceptual view of a rotating transitional boundary layer with system rotation around the axis which is parallel to the leading edge. In the "pressure surface" boundary layer, as illustrated in Fig. 1, the Coriolis force is directed towards the wall and the flow tends to be destabilized. In the "suction surface" boundary layer, in which the direction of Coriolis force is away from the wall, the flow is stabilized.

The governing parameter of the instability in the pressure surface boundary layer is the Görtler number, G_δ, which is defined as

$$G_\delta = Re_\delta \sqrt{Ro_\delta}. \tag{1}$$

Here, Re_δ is the Reynolds number defined as $Re_\delta = U_\infty \delta/\nu$, and Ro_δ is the rotation number defined as $Ro_\delta = \Omega\delta/U_\infty$, where U_∞ is the free-stream velocity and δ is the boundary layer thickness. If G_δ exceeds a certain limit, pairs of counter-rotating streamwise vortices appear, and the lateral heat and mass transfer are expected to be varied. These situations are essentially similar to those of Görtler flow along a concave wall caused by centrifugal force (Görtler, 1940). Extensive discussion on this topic is presented by Guo and Finlay (1994).

To the best of the authors' knowledge, the first approach to the heat transfer problem in connection with the centrifugal instability was reported by McCormack and Keller (1970). They experimentally investigated on the effect of Görtler vortices on heat transfer in the boundary layer along a concave wall. They confirmed the existence of the longitudinal vortices, and showed that there is 100–150% increase in Nusselt number in the presence of vortices.

Kotte (1986) also conducted experiments on the concave wall. He visualized spanwise mass transfer distribution on the surface and also measured the mass transfer coefficient. He showed that mass transfer was indeed increased by the presence of Görtler vortices. However, owing to a lack of velocity distribution information, the Görtler vortices and mass or heat transfer enhancement were not well correlated. He also introduced disturbances via grids of different meshes and found an optimal mesh size for the enhancement of mass transfer.

Crane and Sabzvari (1989) carried out a detailed experiment on a concave wall. They measured both velocity and surface temperature and concluded that Görtler vortices caused both the variation of temperature in the spanwise direction and augmentation of the heat transfer coefficient. They indicated that in the down-wash region where the boundary layer becomes thin due to Görtler vortices, heat transfer was enhanced, and vice versa in the up-wash region.

In an experiment in a rotating frame, Mori et al. (1971) conducted measurements, for the first time, in a circular pipe.

* Corresponding author. Tel.: +81-45-563-1141; fax: +81-45-563-5943.

E-mail address: smasuda@mech.keio.ac.jp (S. Masuda).

0142-727X/00/$ - see front matter
PII: S0142-727X(00)00061-8

Notation

A	surface area of the heater, m^2
G_δ	Görtler number based on Re_δ and Ro_δ
h_x	local heat transfer coefficient, W/m^2K
h_{x0}	local heat transfer coefficient for nonrotating case, W/m^2K
k	thermal conductivity, W/mK
L	length of the flat plate, m
Nu_x	local Nusselt number, $h_x x/k$
Pr	Prandtl number, ν/α
q	total heat flow given by the film heater, W
q_{loss}	total heat loss due to conduction and radiation, W
R, G, B	intensities of Red, Green, Blue
Ra_Ω	rotational Rayleigh number, $\beta L\Omega^2(T_w - T_\infty)L^3/(\nu\alpha)$
Re_δ	Reynolds number, $U_\infty\delta/\nu$
Ro_δ	Rotation number, $\Omega\delta/U_\infty$
T_1, T_2	inlet and outlet temperatures of the test section, K
T_∞	free-stream temperature, $(T_1 + T_2)/2$, K
T_w	local wall temperature, K
U	streamwise mean velocity, m/s
U_∞	free-stream velocity, m/s
u	streamwise fluctuating velocity, m/s
x, y, z	Cartesian coordinates
x_l	length of the flat plate in front of the heater, m

Greeks

α	thermal diffusivity, m^2/s
β	thermal expansion coefficient, K^{-1}
Γ	hue angle, rad
ΔU_{max}	spanwise maximum of velocity difference, m/s
δ	boundary layer thickness, m
λ	spanwise distance of temperature streaks, m
ν	kinematic viscosity, m^2/s
Ω	angular velocity of rotating system, rad/s

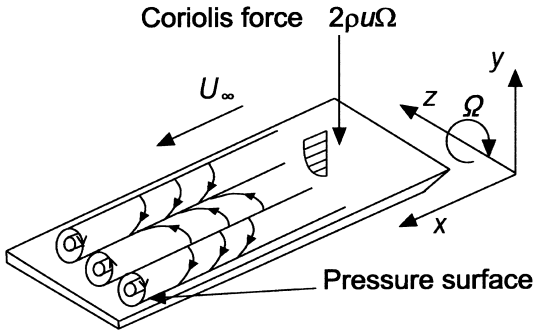

Fig. 1. Conceptual view of rotating boundary layer on pressure surface.

Since this experiment, a great number of investigations have been reported, mainly for application to the cooling of turbine blades (Nomoto et al., 1997).

Among others, the experiment conducted by Wagner et al. (1991) has been the most systematic. They examined the heat transfer in a square-sectioned duct with system rotation, varying both the rotation number and Reynolds number. They concluded that the pressure surface (trailing surface) heat transfer increased compared to the suction surface (leading surface). They inferred that the secondary flow induced by the Coriolis force contributes to an increase in the heat transfer.

There are a number of other experiments, which can be regarded as variants of Wagner et al. experiment, in which, for example, square-sectioned turbulence promoter ribs were set on a duct surface (Taslim et al., 1991), the shape of the duct cross-section was varied (e.g., rectangular and triangular, Harasgama and Morris, 1988), a two or multi-path sectioned duct with sharp corners was used or the thermal boundary condition was changed (Han and Zhang, 1992). However, they are of limited quantitative importance since the results suffer from the secondary flow due to the end-wall boundary layer, the corner effect of a noncircular sectioned duct or, in some cases, turning of the duct centerline. Hence, the results depend on the specific geometry adopted.

In a more recent experiment conducted in a rotating channel, Matsubara and Alfredsson (1996) investigated the influence of the Coriolis force on heat transfer for a wide range of rotation numbers. They confirmed that the temperature field is strongly correlated with the evolution of longitudinal vortices, based on linear stability analysis. Their results suggest the break down of Reynolds analogy between heat and momentum transfer.

In the present experiment, attention has been focused on the pure Coriolis effect directed normal to the wall, in order to obtain universal function for the heat transfer coefficient. For this purpose, we have realized the nominally two-dimensional rotating boundary layer without end-wall contamination, by employing a wind tunnel cross-section with a high aspect ratio, thus eliminating miscellaneous factors such as the end-wall effect, the corner effect and the centrifugal force effect due to curvature.

2. Experimental apparatus and procedure

2.1. Rotating wind tunnel and test plate

Experiments were conducted in an open return-type rotating wind tunnel shown in Fig. 2. It consisted of an inlet duct with a 390 mm × 390 mm cross-section, a two-dimensional contraction with an area ratio of 4.53:1 and a 760 mm × 86 mm × 390 mm test section. These components were mounted on a table 2 m in diameter, which rotates about the leading edge, i.e., parallel to the z-axis, with variable angular velocity Ω up to 20 rad/s.

The room air was supplied by a blower on a stationary frame via a mechanical seal, with the resultant free-stream velocity U_∞ of up to 10 m/s. An acrylic test plate separated the test section into a 390 mm × 40 mm test channel and a bypass channel with 390 mm × 21 mm cross-section. The streamwise pressure gradient was minimized ($-dp/dx \simeq 0$) by adjusting both the wall opposite to the test surface and the flow rate in the bypass channel. The thickness of the test plate was 10 mm, and its leading edge was shaped into a 3.3° wedge with a rounded tip of 0.5 mm diameter. A number of air filters, consisting of mesh and sponge, were installed in the inlet cross-section to decrease the free-stream turbulence level and to trim the flow direction. At the outlet cross-section, also a honeycomb and screens were installed in order to avoid the downstream effects. The resistance of the outlet screen was carefully adjusted so that the oncoming streamline became parallel to the test surface. Due to the limitation on the space, the maintenance of the inlet flow condition was extremely difficult.

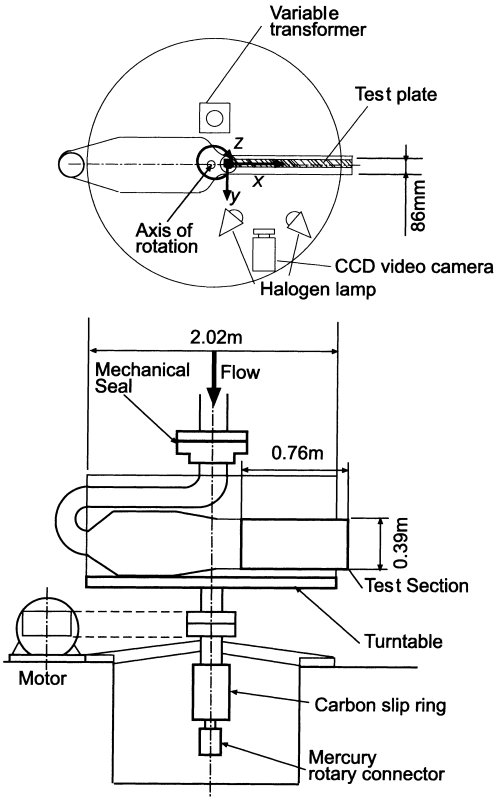

Fig. 2. Experimental setup.

Nevertheless, the free-stream turbulence intensity was always less than 1%, which was sufficiently low for the purpose of the present study.

The test plate had a laminate structure, as shown in Fig. 3. A thermochromic liquid crystal (LC, hereafter) sheet 0.05 mm thick and a stainless steel (SUS304) film 0.01 mm thick were attached to the acrylic plate (10 mm) via adhesive tape (0.01 mm in thickness). The stainless steel film was heated by electric current from a variable transformer mounted on the turntable, to give a uniform heat flux on the test surface. The 600 mm-long heater extended over the test plate. In order to minimize the heat conduction loss to the test plate, a 15 mm-thick styrene foam plate was attached to the back of the acrylic plate. Six pairs of calibrated copper–constantan (CC) thermocouples were set in the back of the stainless steel resistant heater to monitor the time history of the temperature field. The error in the thermocouple measurements is about ±0.05 °C.

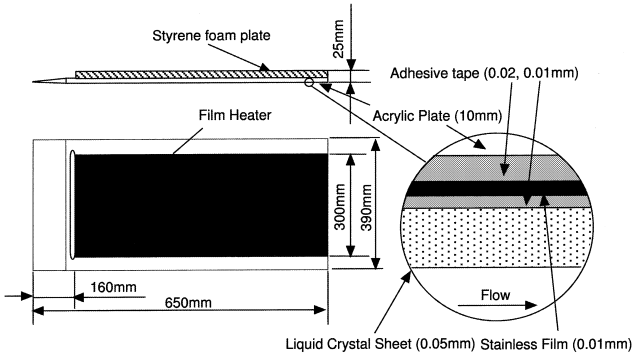

Fig. 3. Details of the test plate.

Since the temperature difference between the wall and the main stream was set to be 10°C, and also angular velocity of the system rotation was 4.6 rad/s at most, the rotational Rayleigh number Ra_Ω was on the order of $O(10^7)$, where Ra_Ω was defined as $\beta L\Omega^2(T_w - T_\infty)L^3/(\nu\alpha)$. Since the buoyancy parameter Ra_Ω/Re^2 appearing in the normalized momentum equation was on the order of $O(10^{-3})$, the buoyancy effect was neglected in the present study.

2.2. Temperature measurements

To measure the temperature distribution on the surface of the test plate, cholesterol induction-type LC was used, with the sensitivity range covering 27–37°C. The color of the LC changed from brown to red to blue, with increasing temperature. The temperature resolution was about 0.02°C and the space resolution was sufficiently high for recognizing the surface temperature distribution due to vortex formation.

The color distribution image of the LC layer resulting from the streamwise vortices was photographed using a digital video camera employing 3 CCD's. The LC sheet was illuminated by two halogen lamps each with a power of 75 W. The image obtained covered 100 mm × 360 mm on the plate, which corresponded to about 100 300 pixels.

Since the image of the LC was strongly dependent on the optical conditions, such as location and setting of the camera and light source, special attention was paid to keep them constant throughout both the LC calibration and the main experiment. The correlation curve between the color image of LC and the surface temperature was obtained by evaluating the hue angle Γ, which responds to the temperature variation almost linearly (Dabiri and Gharib, 1997). To evaluate Γ, the LC images were first saved in a personal computer in a binary bitmap file in which the intensities of three color elements, i.e., red (R), green (G) and blue (B), were stored for each pixel. From the R, G, B data, Γ was evaluated as

$$\Gamma = \begin{cases} \theta & g \geqslant b, \\ 2\pi - \theta & g < b, \end{cases} \tag{2}$$

where

$$\theta = \frac{\cos^{-1}(2r - g - b)}{\sqrt{6c}}$$

and

$$r = \frac{R}{R+G+B},$$
$$g = \frac{G}{R+G+B},$$
$$b = \frac{B}{R+G+B},$$
$$c = \sqrt{\left(r - \frac{1}{3}\right)^2 + \left(g - \frac{1}{3}\right)^2 + \left(b - \frac{1}{3}\right)^2}.$$

The calibration device shown in Fig. 4 was used to correlate the color information Γ with temperature. It consisted of a 38 W film heater and an electronic cooler mounted on each end of the 5 mm-thick copper plate. After generating a linear temperature gradient using these heat and cold sources, temperature was measured by five pairs of CC-thermocouples along the plate and the LC image was simultaneously taken. The unique correlation between Γ and surface temperature T_w was obtained in this manner, as shown in Fig. 5. The major sources of error in the temperature measurements using the calibrated LC were considered to be: (1) uncertainty in thermocouple output; (2) optical error such as viewing angle or the intensity

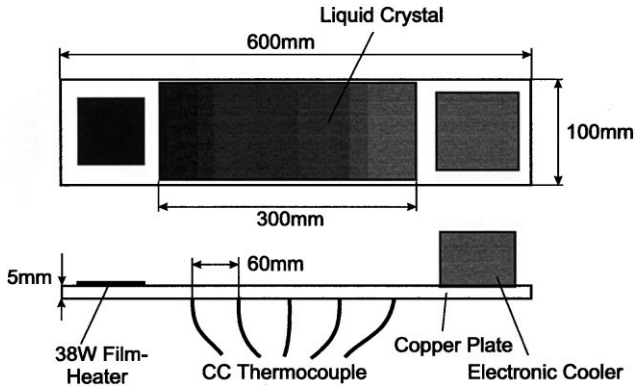

Fig. 4. Schematics of the calibration device.

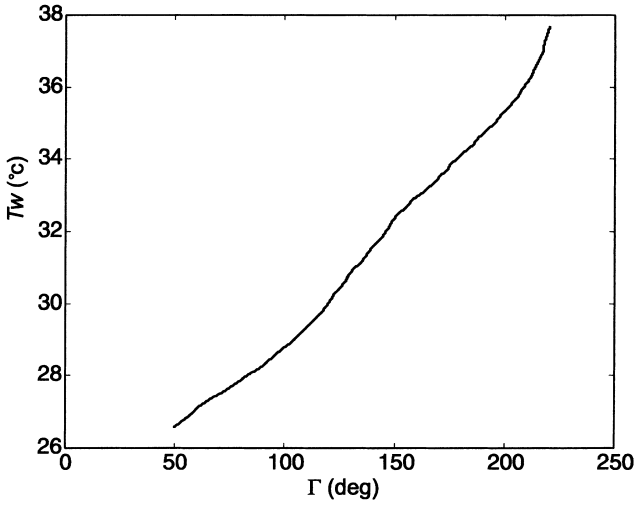

Fig. 5. Hue-temperature calibration curve.

of the light source; (3) evaluation of the calibration curve itself. Considering all these factors, the total error of the temperature measurements on the LC was estimated to be approximately ±0.3°C.

Two pairs of CC-thermocouples were set in the free-stream to measure the temperature outside the thermal boundary layer. In order to monitor the streamwise temperature change, the temperature was measured at two locations, one near the leading edge ($T_1, x = 50$ mm) and the other downstream ($T_2, x = 650$ mm).

The local heat transfer coefficient h_x is calculated as

$$h_x = (q - q_{\text{loss}})/(T_w - T_\infty)A. \quad (3)$$

In this equation, q indicates the total heat flow which is assumed to be equal to the electric power applied to the heater (voltage × current). T_w is the local wall temperature, $T_\infty = (T_1 + T_2)/2$ the free-stream temperature, A the surface area of the heater and q_{loss} accounts for the heat loss due to both heat conduction to the back plate and radiation. In the present experiments, the heat flow q given by the heater was about 150 W/m^2. The area A was 100 mm × 1800 mm, namely, the total span of the heating section was divided into three 100 mm-wide sections which were electrically connected in series. The uncertainties in this heat transfer coefficient is estimated to be about 20% in the far-upstream region and 10–5% in the downstream region.

2.3. Velocity measurements

To investigate the velocity distribution, we used a single-element hot-wire probe and a custom-made constant-temperature anemometer (CTA) (Matsubara and Alfredsson, 1998), both of which were mounted on the turntable. A two-dimensional automatic traversing mechanism enabled remote-controlled measurement, as the hot-wire was continuously traversed in the wall-normal direction y and the spanwise direction z. In the streamwise direction x, the traversing stage was moved by hand.

A silver-coated Rt · Rh wire (Wollaston wire) was used for the sensing element of the hot-wire probe. The sensor diameter was 2.5 μm and length was 0.5 mm. The transmission of the electric signal between the rotating and stationary frames, as well as the power supply from the stationary frame, was realized by employing a 19-pole carbon slip ring device and 4-pole mercury rotary connector which is hard to suffer from noise. The former was mainly used for transmitting digital output signal to control stepping motor, and the latter for supplying AC100 V electric power to the rotating table and transmitting CTA signal.

Data sampling using the CTA and CC-thermocouple output, as well as control of the traversing system, was performed with a 32-bit personal computer. For the velocity measurement, typical sampling frequency was 5 kHz and sampling time was 2 s. In order to remove the noise, AC output signal from CTA (corresponding to the velocity signal) was amplified by 20 dB. The measurements achieved spatial resolutions of 0.5 mm and 1.0 mm in the y- and z-directions, respectively.

3. Results and discussion

3.1. Base flow experiment

Prior to the experiment under the rotating condition, the two-dimensionality of the flow and surface temperature distribution was examined in the nonrotating state. Velocity contours in the y–z plane at $x = 0.25$ m, taken at $U_\infty = 4$ m/s, are shown in Fig. 6. The contour lines are parallel to the z-axis, confirming that the flow is uniform in the spanwise direction. Fig. 7 shows the velocity profile at the same x-position. The Blasius profile is shown by the dashed line for reference. The plots are in good agreement with the Blasius profile, indicating the insignificance of the pressure gradient. The maximum deviation from the Blasius profile was found to be ±0.5% over at least 40% of the channel span, therefore the base flow is sufficiently uniform to detect the spanwise velocity variation due to the system rotation. Inspection of the LC image taken under the nonrotating condition also confirmed the temperature distribution to be uniform in the spanwise direction (cf. Fig. 8(a)).

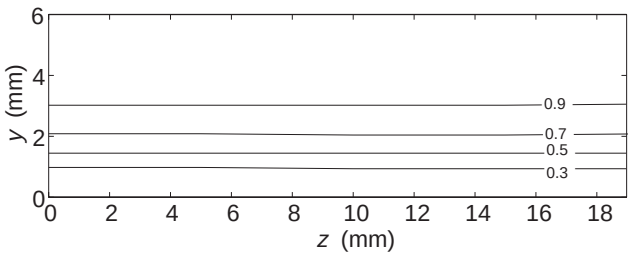

Fig. 6. Mean velocity contour plot at y–z plane at $x = 0.25$ m, $U_\infty = 4$ m/s. Contour spacing is 0.2 in u/U_∞.

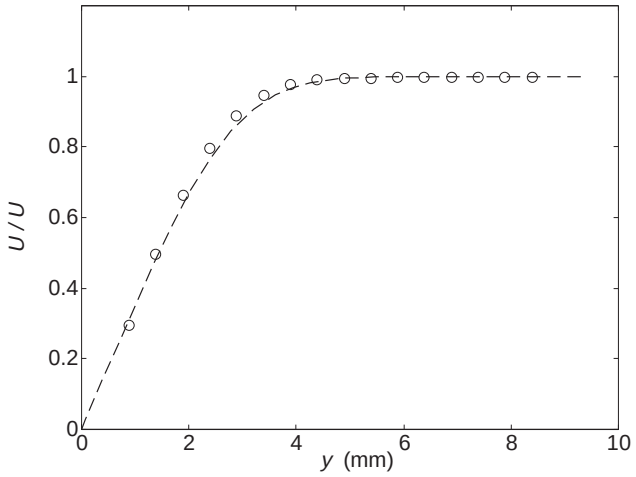

Fig. 7. Mean velocity profile at $x = 0.25$ m, $U_\infty = 4$ m/s, $\Omega = 0$ rad/s. ○: Experimental data; dashed line: Blasius' analytical profile.

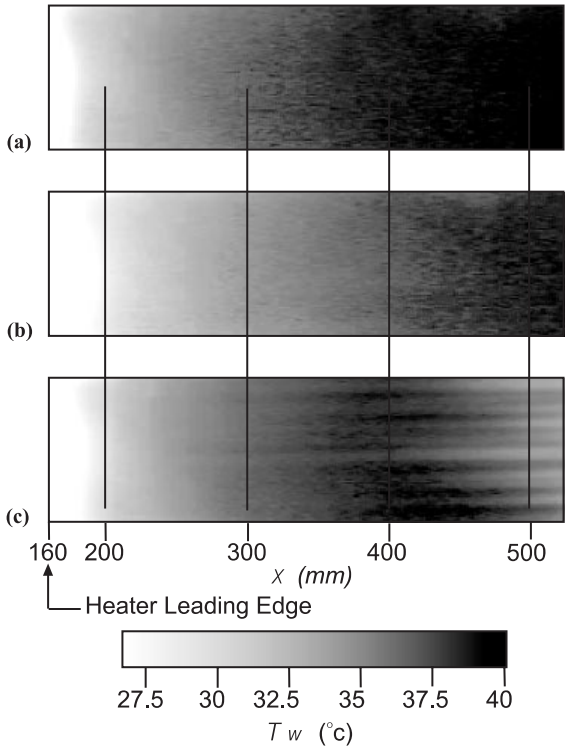

Fig. 8. Surface temperature distribution without humps: (a) nonrotation; (b) suction surface; (c) pressure surface. Flow is from left to right, $U_\infty = 4$ m/s, $\Omega = 4.6$ rad/s.

3.2. Heat transfer experiment: unconstrained flow

As explained later in detail, the experiments have been performed under two conditions: the flow with and without constraint to the longitudinal vortex position. Here, the results are presented for the unconstrained condition, where the measurements were performed without applying any artificial disturbance to the base flow. The free-stream velocity was kept constant at $U_\infty = 4$ m/s throughout.

The temperature distribution without system rotation (cf. Fig. 8(a)), shows the lowest temperature at the upstream end of the heater (left end of the picture) and a gradual increase downstream, simultaneously demonstrating the spanwise uniformity. The temperature distribution seems to be unaltered on the suction surface at $\Omega = 4.6$ rad/s (cf. Fig. 8(b)). On the pressure surface, however, the temperature distribution is quite different as shown in Fig. 8(c), which is a result of changing the direction of rotation while keeping the rotation rate constant. Regions of high and low temperatures, as indicated by the light and dark streaks, appear irregularly in space towards the downstream region, $x \geqslant 0.3$ m (corresponding to $G_\delta \geqslant 115$). This alternating dark/light pattern is called "temperature streaks" hereafter. The width of the streak pattern is about 9 mm on average, though there is considerable scatter.

3.3. Heat transfer experiment: constrained flow

Considering the results of the heat transfer experiment in a concave wall boundary layer, conducted by Crane and Sabzvari (1989), it is expected that the present temperature streaks are also caused by streamwise vortices. To elucidate the correlation between the temperature streaks and streamwise vortices, it is necessary to perform the measurements of temperature and velocity simultaneously. However, the velocity measurement using hot-wire anemometer in a varying temperature field is erroneous and, since the time constant of the liquid crystal system is large compared to that of the variation of the temperature streak, it is more efficient to control the flow so that the same condition can be repeatedly created. To this end, a device that fixes the spanwise location of the temperature streaks is introduced.

From previous experiments conducted by the present authors' group, it is known that weak nonuniformity introduced near the leading edge effectively fixes the spanwise location of the streamwise vortices without altering the base flow (Matubara and Masuda, 1991; Masuda et al., 1994). In the present study, the disturbance has been generated by mounting a spanwise array of tiny humps of 0.5 mm high, shown in Fig. 9, onto the test surface at $x = 10$ mm. The distance between the humps is $\lambda = 9$ mm, which is equal to the mean spanwise spacing of temperature streaks observed in the experiment under the conditions without constraint (Fig. 8).

Fig. 10 shows the temperature distribution obtained under the constrained condition. On the pressure surface, there are some differences compared with results of the experiment without humps shown in Fig. 8. Namely, the temperature streaks appear from far upstream, align more regularly at the spanwise position of the humps, and appear more clearly. Note that in Fig. 10(a), the results for the nonrotation case as well as the suction surface show no indication of the effect of the wake of the humps.

3.4. Velocity field

To examine the generation mechanism of the temperature streaks, the velocity was measured at five streamwise positions

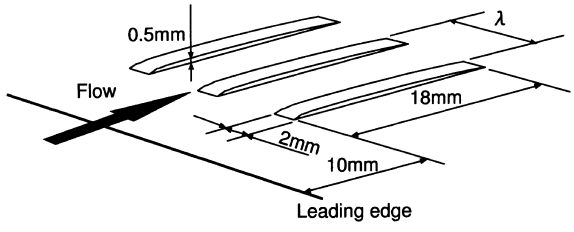

Fig. 9. Shape of humps.

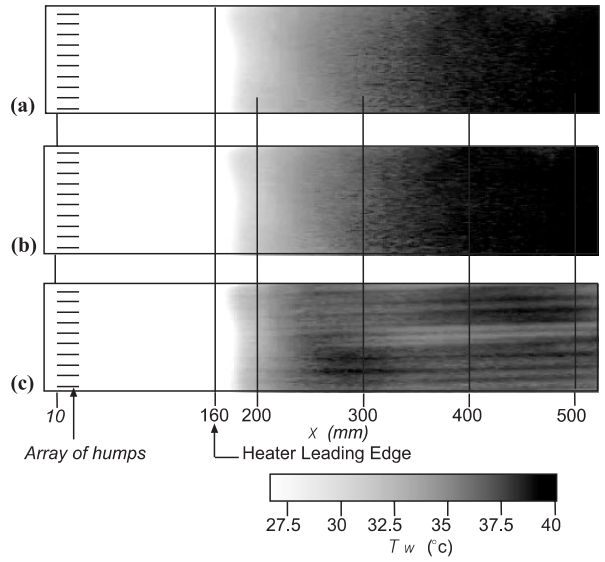

Fig. 10. Surface temperature distribution under "the constrained condition": (a) nonrotation; (b) suction surface; (c) pressure surface. Flow is from left to right, $U_\infty = 4$ m/s, $\Omega = 4.6$ rad/s.

by traversing the I type single hot-wire probe in y- and z-directions and measure the streamwise velocity component. Fig. 11 shows contour plots of the mean velocity on the pressure side, in which the theoretically estimated boundary layer thickness is given by the symbol δ at the right margin of each figure, and the spanwise positions of the humps are marked by the triangles at the bottom.

In the measurements with system rotation, the velocity measurement might be contaminated by the velocity components normal to x-axis, though the amount of error due to this effect is hard to estimate. The subsequently presented results of the velocity distribution under the influence of Coriolis force should be restricted to qualitative discussion.

The velocity contours at $x = 130$ mm ($G_\delta = 59$) exhibit small deceleration near the spanwise position of the humps. It is worth noting that there is no such distortion in the nonrotation case even if the humps are applied; this pattern is only seen in the pressure surface boundary layer. The distortion of the velocity contours becomes more pronounced downstream, extending beyond the outer edge of the boundary layer, and tends to form a mushroom-like shape with the closed region of the low-speed portion ($z \sim 8$ mm) away from the wall. These regions are presumably related to the up-wash motion brought about by counter-rotating pairs of streamwise vortices. Such motion is indicated by broken lines in the velocity contour plot for the cross section at $x = 410$ mm, Fig. 11(d). On both sides of the low-speed region, the boundary layer becomes appreciably thin, implying a down-wash caused by the vortices.

At $x = 450$ mm ($G_\delta = 150$), the size of the low-speed region further increases, while the velocity deficit shown by the low-speed portion decreases, indicating the decay of the streamwise vortices. As a measure of the vortex strength, the maximum of velocity difference in spanwise direction at a given height y, $\Delta U_{\max}/U_\infty$, is plotted in Fig. 12. As seen in this figure, the velocity defect increases linearly until $G_\delta \leqslant 119$ ($x \leqslant 0.33$ m) and decays gradually thereafter.

In Fig. 13, the contours of velocity fluctuations at the same streamwise location are compared. In small G_δ stage ($G_\delta = 59$ and 90), the turbulent intensity is below 1% and there is no prominent velocity fluctuation. At $G_\delta = 119$ ($x = 330$ mm), where $\Delta U_{\max}/U_\infty$ reaches its maximum, velocity fluctuation appears at the shoulder and stem of the mushroom-shaped pattern and increases rapidly downstream. These rapid increments of turbulence levels may be attributable to the occurrence of secondary instability (Masuda et al., 1994), though the available information is too limited to support this relationship. At $G_\delta = 150$ ($x = 450$ mm), the high velocity fluctuated region is getting larger and the velocity field is mostly flattened, indicating the transition to turbulence.

In order to consider the relationships between the temperature streaks and streamwise longitudinal vortices, the spanwise variation of wall temperature at $x = 410$ mm is shown in Fig. 14. Compared with the velocity contour, although there is some scatter, the temperature distribution exhibits spanwise periodicity, with the length scale λ of about 9 mm. More

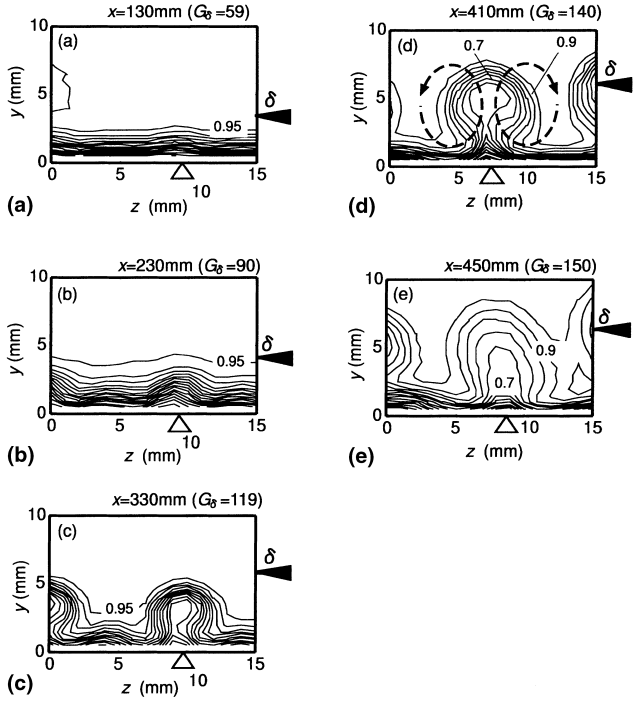

Fig. 11. Distribution of mean streamwise velocity on the pressure surface ($U_\infty = 4$ m/s, $\Omega = 4.6$ rad/s). Contour spacing is 0.05 in u/U_∞. △: position of humps.

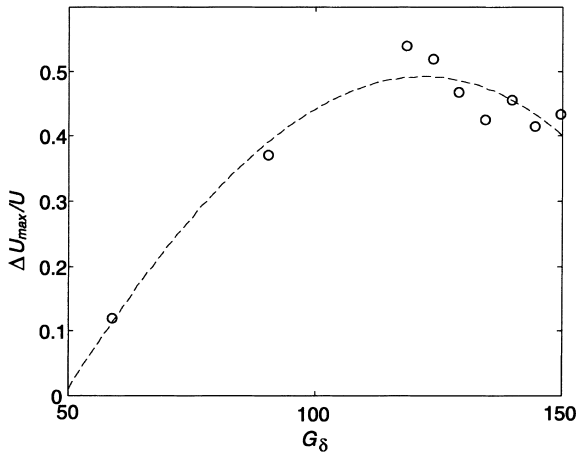

Fig. 12. The distortion of velocity distribution due to longitudinal vortices (constrained state).

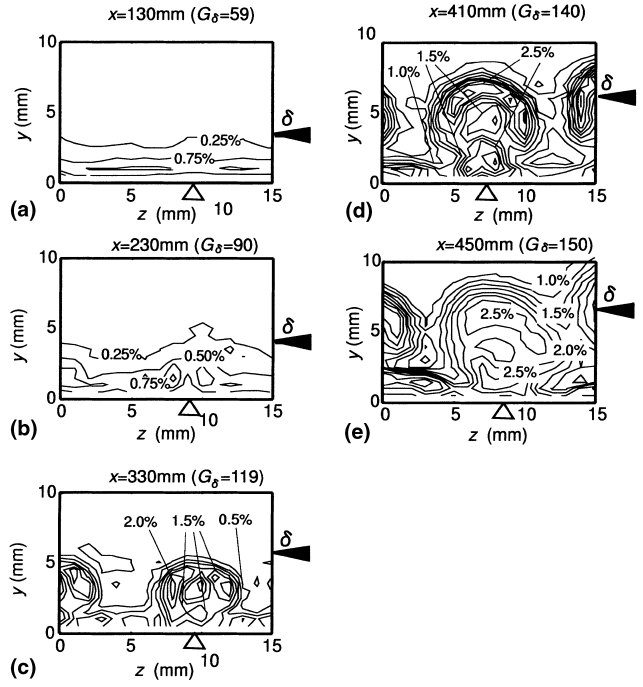

Fig. 13. Contour plots of velocity fluctuation on the pressure surface ($U_\infty = 4$ m/s, $\Omega = 4.6$ rad/s). Contour spacing is 0.25% in u/U_∞. △: position of humps.

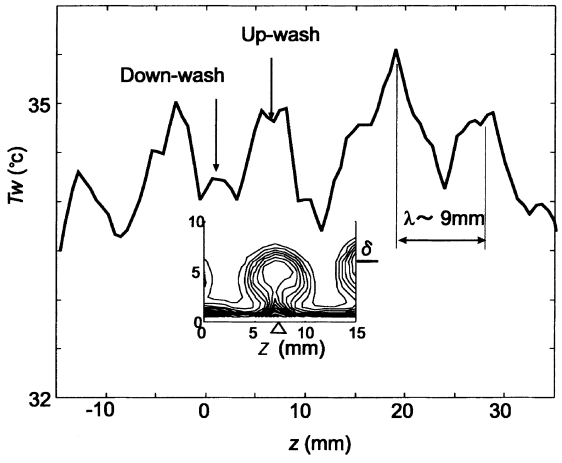

Fig. 14. Spanwise temperature distribution at $x = 0.41$ m compared with the velocity contour.

importantly, the spanwise temperature peak corresponds exactly to the low-velocity region, while the temperature valley corresponds to the high-speed region. Based on these images, it is concluded that the streamwise vortices caused by the system rotation transport the high-momentum, low-temperature fluid towards the wall (down-wash), which generates a thinner boundary layer with a steep temperature gradient at the wall. Furthermore, the low-momentum, high-temperature portions of fluid near the wall merge along the wall due to the streamwise vortices, making the boundary layer thicker and wall temperature gradient smaller.

3.5. Heat transfer coefficient

Using the data obtained from the LC image, the local heat transfer coefficient, defined by Eq. (3), is now calculated. Since the heat flux is approximated as the electric power supplied to the heater, the heat loss q_{loss} in Eq. (3) should be estimated and compensated before discussing the effect of system rotation on the heat transfer coefficient. To this end, the analytical solution was consulted. According to Kays (1966), the local Nusselt number of a laminar boundary layer developing on a stationary (nonrotating) flat plate with uniform heat flux at a finite distance from the leading edge can be expressed as

$$Nu_x = \frac{h_x x}{k} = 0.453 Pr^{1/3} Re_x^{1/2} \left[1 - \left(\frac{x_l}{x}\right)^{3/4}\right]^{-1/3}, \quad (4)$$

where x is the distance from the leading edge, x_l the distance from the front of the thermal boundary layer, k the thermal conductivity of the fluid, and Prandtl number $Pr(= \nu/\alpha)$ is 0.72 for air.

The measured heat transfer coefficient without rotation is shown with results for Eq. (4) in Fig. 15. The measured data are higher by a constant amount than the theoretical result, except at the beginning of heating. This difference in the coefficient is assumed to correspond to the amount of heat loss by conduction and radiation, and hence is subtracted from the original data for the all measurements. The compensated heat transfer coefficient agrees well with the theoretical one except near the leading edge. The heat loss due to radiation and conduction to the wall are estimated to be about 2% and 50% of given heat flux, respectively. Although the amount of heat loss may vary when the channel is rotated, the data are corrected in the same manner for the subsequent results. A precise estimation of the heat loss is the task of the future experiments.

The spanwise-mean heat transfer coefficient h_x, normalized by the nonrotation value h_{x0}, is plotted in Fig. 16. Under the condition without humps, h_x remains at nearly the same level as h_{x0} in the upstream region $x \leqslant 0.4$ m. h_x then increases dramatically further downstream, and the location of the steep increase is coincident with the appearance of the temperature streaks seen in Fig. 8. At the downstream end of the test section, h_x becomes as high as 180% of h_{x0}. Under the condition with the humps, the increase of h_x begins far upstream ($x \geqslant 0.24$ m). This region exhibits the linear increase of the spanwise velocity difference as shown in Fig. 12 as well as in Fig. 11(a)–(c). In the region further downstream ($0.35\text{ m} \leqslant x \leqslant 0.47$ m), h_x levels off once. This corresponds to the decrease in the velocity deficit due to the decay of the

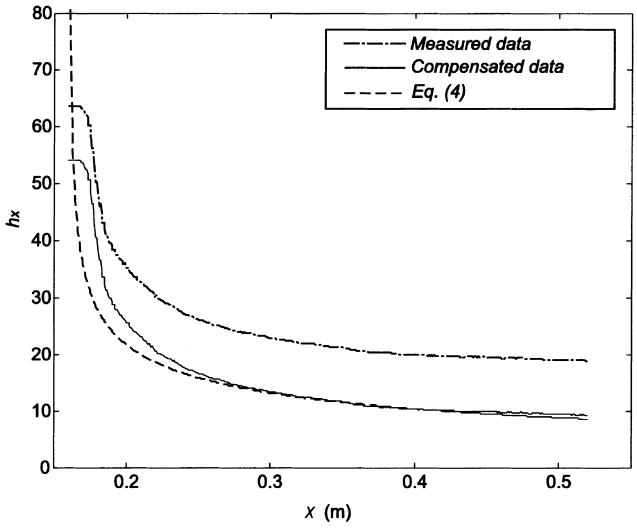

Fig. 15. Analytical solution of local heat transfer coefficient for nonrotating laminar boundary layer and experimental data.

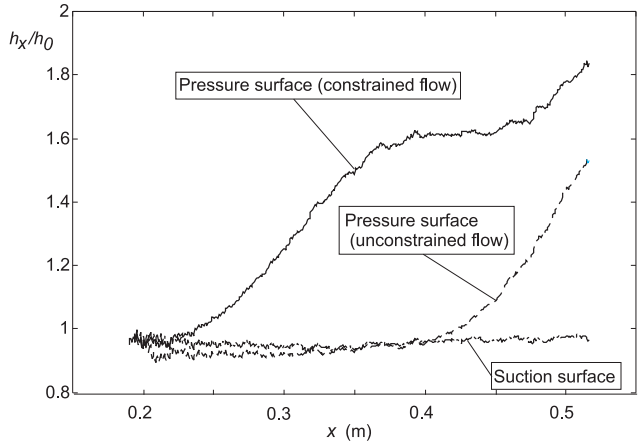

Fig. 16. Spanwise-mean heat transfer coefficient on pressure and suction surface.

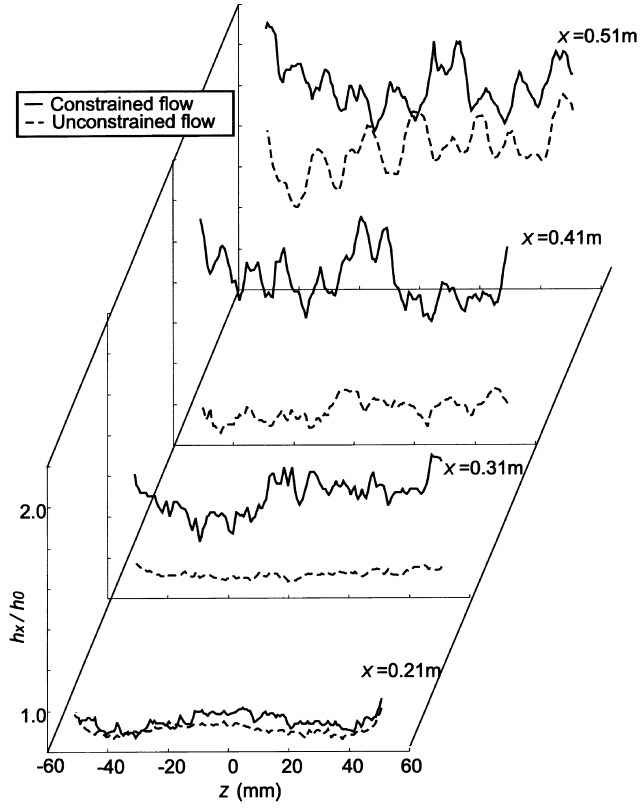

Fig. 17. Spanwise local heat transfer coefficient on pressure surface with and without humps.

streamwise vortices, as already seen in Figs. 11(d), (e) and 12. h_x again increases further downstream ($x \geqslant 0.45$ m). This is probably attributable to the high-frequency fluctuation before the breakdown to turbulence, as seen in Fig. 13(e), though this is not yet clear because of a lack of detailed information on this downstream region.

Nevertheless, it is worth noting that the significant increase in the heat transfer coefficient in the constrained experiment suggests the usefulness of an array of tiny humps as a means of heat transfer augmentation on the pressure surface. On the contrary, the heat transfer coefficient on the suction surface is essentially unaltered by system rotation. This is because the Coriolis force acting away from the wall has no effect on the generation of the streamwise vortices, and it tends to smooth out the initial spanwise nonuniformity, hence maintaining the original two-dimensional laminar condition (turbulent intensity is below 1% and the heat transfer coefficient is same as the stationary laminar case).

The spanwise variation of the local heat transfer coefficient is shown in Fig. 17, for the results of experiments with and without humps at four streamwise positions. Note that the heat transfer coefficient h_x is normalized by the spanwise-average value for the nonrotation case at the corresponding streamwise positions. At $x = 0.21$ m, the spanwise variation in both cases is negligible. However, from $x = 0.31$ m, the variation is gradually amplified, and, especially at $x = 0.51$ m, the minimum is about 25% of the maximum in both cases. It is clear that the constrained condition achieves higher heat transfer rates at all locations as compared with those without the constraints. The present results suggest that the effective use of the longitudinal vortices can provide efficient heat transfer devices that operate in rotating systems.

4. Concluding remarks

The heat transfer characteristics of a transitional boundary layer on a flat plate subjected to Coriolis force have been experimentally investigated under constant heat flux. The experiments were conducted in a rotating wind tunnel with a free-stream velocity of 4 m/s, free-stream turbulence level below 1% and angular system rotation velocity 4.6 rad/s. A liquid crystal sheet was employed for the quantitative visualization of temperature distribution on the plate. A single hot-wire sensor and automatic traversing mechanism enabled the velocity distribution to be obtained on several cross-sections.

The major conclusions are as follows:

- In the pressure surface boundary layer, in which Coriolis force acts perpendicularly towards the wall, high- and low-temperature streaks appear. Their spanwise position closely coincides with the spanwise structure in streamwise velocity profiles.
- The spanwise-average local heat transfer coefficient was increased by 80% relative to that in the non-rotation case. The local heat transfer coefficient increases downstream up to certain distance from the leading edge. This variation is well related with the increase in the distortion of streamwise mean velocity profiles as a consequence of the development of longitudinal vortices.
- Upon introducing a spanwise array of tiny humps, the heat transfer rate dramatically increased from the far upstream as compared to the case without humps. This suggests that the humps are useful as a means of heat transfer augmentation on the pressure surface.
- On the suction surface, the heat transfer coefficient was essentially unaltered by the system rotation. This is because the Coriolis force away from the wall tends to smooth out the initial spanwise non-uniformity and diminishes the streamwise vortices, maintaining the original, two-dimensional laminar condition.

Acknowledgements

Financial support for the present study has been provided by the Ministry of Education, Science and Culture, through grant-in-aid for Scientific Research, No. 11650189. Thanks are due to Mr. H. Komiyama and Dr. M. Matsubara for taking

part in constructing parts of the experimental equipment and conducting the experiment.

References

Crane, R.I., Sabzvari, J., 1989. Heat transfer visualization and measurement in unstable concave-wall laminar boundary layers. ASME J. Turbomachinery 111, 51–56.

Dabiri, D., Gharib, M., 1997. Digital particle image thermometry: The method and implementation. Exp. Fluids 119, 20–29.

Görtler, H., 1940. Über eine dreidimensionale Instabilität laminarrer Grenzschichten an konkaven Wänden. Göttingen Nachr. Math. Phys. Kl 2, 1.

Guo, Y., Finlay, W.H., 1994. Wavenumber selection and irregularity of spatially developing nonlinear dean and Görtler vortices. J. Fluid Mech. 264, 1–40.

Han, J.C., Zhang, Y.M., 1992. Effect of unevern wall temperature on local heat transfer in a rotating square channel with smooth walls and radial outward flow. ASME J. Heat Transfer 114, 850–859.

Harasgama, S.P., Morris, W.D., 1988. The influenced of rotation on the heat transfer characteristics of circular, triangular and square-sectioned coolant passages of gas turbine rotor blades. ASME J. Turbomachinery 110, 44–50.

Kays, W.M., 1966. Convective Heat and Mass Transfer. McGraw-Hill, New York.

Kotte, V., 1986. Taylor–Görtler Vortices and their effect on heat and mass transfer. In: Proceedings of the Eighth International Heat Transfer Conference, San Francisco, CA, pp. 1139–1144.

McCormack, P.D., Keller, M., 1970. Taylor–Görtler vortices and their effect on heat transfer. ASME J. Heat Transfer 92, 101–112.

Masuda, S., Hori, D., Matsubara, M., 1994. Secondary instability associated with streamwise vortices in a rotating boundary layer. IUTAM Symposium Laminar-Turbulent Transition, pp. 69–76.

Matsubara, M., Alfredsson, H., 1996. Experimental study of heat and momentum transfer in rotating channel flow. Phys. Fluids 8, 2964–2973.

Matsubara, M., Alfredsson, H., 1998. Secondary instability in rotating channel flow. J. Fluid Mech. 368, 27–50.

Matubara, M., Masuda, S., 1991. Three-Dimensional instability in rotating boundary layer. ASME FED, Boundary Layer Stability and Transition to Turbulence 114, 103–107.

Mori, Y., Fukuda, T., Nakayama, W., 1971. Convective heat transfer in a rotating radial circular pipe (2nd Report). Int. J. Mass Heat Transfer 14, 1807–1824.

Nomoto, H., Koga, A., et al., 1997. The advanced cooling technology for the 1500°C class gas turbines: steam-cooled vanes and air-cooled blades. ASME J. Eng. Gas Turbines Power 119, 624–632.

Taslim, M.E., Rahman, A., Spring, S.D., 1991. An experimental investigation of heat transfer coefficients in a spanwise rotating channel with two opposite rib-roughened walls. ASME J. Turbomachinery 113, 75–82.

Wagner, J.H., Johnson, B.V., Hajak, T.J., 1991. Heat transfer in rotating passages with smooth walls and radial outward flow. ASME J. Turbomachinery 113, 42–51.